

Article

Designing Incidence-Angle-Targeted Anti-Cavitation Foil Profiles Using a Combination Optimization Strategy

Di Zhu ^{1,2}, Ruofu Xiao ^{1,2,*}, Ran Tao ^{2,3} and Fujun Wang ^{1,2}

¹ College of Water Resources and Civil Engineering, China Agricultural University, Beijing 100083, China; zhu_di@cau.edu.cn (D.Z.); wangfj@cau.edu.cn (F.W.)

² Beijing Engineering Research Center of Safety and Energy Saving Technology for Water Supply Network System, China Agricultural University, Beijing 100083, China; randytao@mail.tsinghua.edu.cn

³ Department of Energy and Power Engineering, Tsinghua University, Beijing 100083, China

* Correspondence: xrf@cau.edu.cn

Received: 15 October 2018; Accepted: 5 November 2018; Published: 9 November 2018



Abstract: In hydraulic machinery, the surface of the blade can get damaged by the cavitation of the leading-edge. In order to improve the cavitation performance, the anti-cavitation optimization design of blade leading-edge is conducted. A heuristic-parallel locally-terminated improved hill-climbing algorithm, which is named as the global dynamic-criterion (GDC) algorithm was proposed in this study. The leading-edge shape of NACA 0009-mod foil profile was optimized by combining the GDC algorithm, CFD prediction, Diffusion-angle Integral (DI) design method and orthogonal test. Three different optimal foil geometries were obtained for specific incidence angles that 0, 3, and 6 degrees. According to the flow field analyses, it was found that the geometric variation of the optimized foil fits the incoming flow better at the respective optimal incidence angles due to a slighter leading-edge flow separation. The pressure drops become gentler so that the cavitation performance get improved. Results show that the GDC algorithm quickly and successfully fits the target condition by parallel running with the ability against falling into local-best tarps. The $-C_{pmin}$ of the optimal foils was improved especially by +11.4% and +14.5% at 3 and 6 degrees comparing with the original foil. This study provided a reference for the anti-cavitation design of hydraulic machinery blades.

Keywords: leading edge; global optimization; cavitation inception; orthogonal test; CFD simulation

1. Introduction

Leading-edge (LE) cavitation is the most common type of cavitation in hydraulic machinery [1,2]. The occurrence of LE cavitation is strongly related to the pressure changes generated by fluid flow around the geometry [3,4]. The direct effect of geometric shape on LE cavitation will be considered in the design of blades or other flow-around bodies. The cavity or traveling bubbles of LE cavitation often covers the surface [5] which may cause direct material damage due to the collapse of cavitation bubbles [6]. Therefore, it is very important to investigate and improve the LE cavitation (including delaying its occurrence, reducing its size, etc.) for the design of hydraulic machinery [7–9]. Compared with the design of the flow passage, the blade will exert a direct force on the fluid medium while working and generate a pressure difference between the two sides of blade surface [10–12]. The blade cavitation, especially the LE cavitation characteristics, has become a key factor restricting the blade design under specific conditions. In the past, many researchers have studied the occurrence and characteristics of LE cavitation [13–15]. Generally, cavitation occurs when pressure drops below the saturation pressure. Because of the flow separation and local pressure drop at the blade LE, cavitation often occurs at the LE [16]. Experimental studies found that the development of the cavity had a

negative effect on the flow separation due to inter-phase surface tension [17]. The interaction effect causes a special relationship between the separation position and cavitation inception position in the laminar flow case around a smooth body [18]. This relationship will be different in turbulent flow case, rough surface case and other different boundary layer cases [19]. Generally, the flow separation and pressure drop caused by the geometric characteristics of blade LE will regularly affect the occurrence and development of cavitation at a certain incidence angle [20].

Foil was commonly used as the simplified model of hydraulic machinery blades in engineering [21]. Meanline-symmetrical foils can further reduce the complexity of geometric parameters and improve the pertinence of the research [22]. The smooth symmetrical NACA0009 foil profile can be used to study the laminar flow under a certain Reynolds number. NACA0009 and its modified profiles are popular in the former studies of hydrodynamics and hydraulic machinery including the LE cavitation, tip-clearance cavitation, wake and hydraulic damping, excitation and response [23,24]. Also, numerous researches have been carried out on the LE cavitation of hydraulic machineries [25–30].

Based on the study of LE cavitation on foils and turbo blades, there have been abundant researches on the mechanism, occurrence, development and variation. However, there is still a problem that has not been solved perfectly that how to obtain a hydraulic geometry for improving the LE cavitation. Optimization is an effective way to solve this problem by properly defining the optimized target and choosing the reasonable algorithm. In this study, the foil shape with better LE cavitation characteristics was set as the optimization target. Feasible algorithms including genetic algorithm, ant colony algorithm, hill climbing algorithm, etc. can be used. Each of them has its own advantages and disadvantages and requires improvements or adjustments in different cases [31–35]. Huang et al. [36] used the genetic algorithm to drive the computational fluid dynamics simulations, guiding the configuration of a suction jet and a blowing jet on the airfoil's upper surface. Liu et al. [37] selected an adaptive simulated annealing algorithm to solve the energy performance calculation model. The weighted average efficiency of the impeller after the three-condition optimization has increased by 1.46% than that of original design. Liu et al. [38] used a multi-objective optimization design system to develop an ultrahigh-head runner with good overall performance. Compared to the initial runner, the preferred runner's efficiency under turbine mode is increased by about 0.7% and the pump efficiency by about 0.6%, while the runner's cavitation is greatly promoted. Liu et al. [39] proposed the hydraulic design method of controllable blade angle for rotodynamic multiphase pump with impeller and diffuser. The orthogonal optimization method was employed to optimize the geometry parameters. The distributions of gas volume fraction and the pressure became more uniform after optimization, and improved the transporting performance of the multiphase pump. In this study, the global dynamic-criterion (GDC) algorithm which can run in parallel, stop from dropping into local-best trap was chosen. Finally, reducing the number of effective tests and reducing time cost is the top priority of engineering optimization. Therefore, the strategy combining the GDC algorithm, CFD prediction, Diffusion-angle Integral (DI) method [40] for foil thickness geometry design and orthogonal test was used for optimization. The new optimization algorithm proposed in this paper can complete the optimization process quickly and simply with high optimization efficiency. Based on the strategy above, the optimal hydraulic shape and improved cavitation performance of NACA0009 foil can be obtained at different specific incidence angles. This research shows an example for designing the anti-cavitation turbo blade of hydraulic machinery including axial-flow pump, mixed-flow pump, centrifugal pump and other bladed pumps.

2. The Studied Hydrofoil Object

The NACA0009-mod profile was used as the objective hydrofoil [24]. As shown in Figure 1, it is a symmetrical foil, m is the meanline direction and t is the thickness. The total meanline length is $m_{total} = L$. The thickness t distribution along m direction can be expressed as:

$$\begin{cases} \frac{t}{L} = a_0\left(\frac{m}{L}\right)^{\frac{1}{2}} + a_1\left(\frac{m}{L}\right) + a_2\left(\frac{m}{L}\right)^2 + a_3\left(\frac{m}{L}\right)^3 & 0 \leq \frac{m}{L} \leq 0.5 \\ \frac{t}{L} = b_0 + b_1\left(1 - \frac{m}{L}\right) + b_2\left(1 - \frac{m}{L}\right)^2 + b_3\left(1 - \frac{m}{L}\right)^3 & 0.5 \leq \frac{m}{L} \leq 1 \end{cases} \quad (1)$$

where

$$\begin{cases} a_0 = +0.1737 \\ a_1 = -0.2422 \\ a_2 = +0.3046 \\ a_3 = -0.2657 \end{cases} \quad \begin{cases} b_0 = +0.0004 \\ b_1 = +0.1737 \\ b_2 = -0.1898 \\ b_3 = +0.0387 \end{cases} \quad (2)$$

The hydrofoil was built based on Equations (1) and (2), and another trailing edge modification. The TE modification was cut on the trailing edge to $l = 0.9091L$. The TE was processed by circular arc, and the radius is $r = 0.0168L$. The final hydrofoil model is shown in Figure 1. The incidence angle was defined as α . The 2D flow domain ($1.5l \times 7.5l$) for computational fluid dynamics (CFD) simulations was built as shown in Figure 2. The commercial software ANSYS CFX was used for numerical simulation.

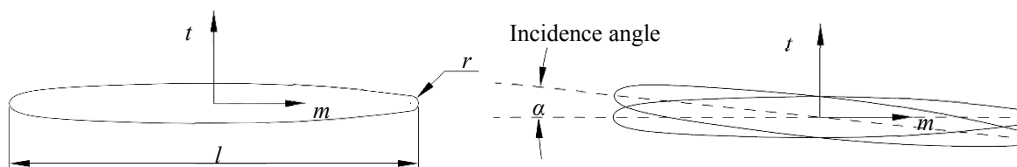


Figure 1. Hydrofoil model and its parameters.

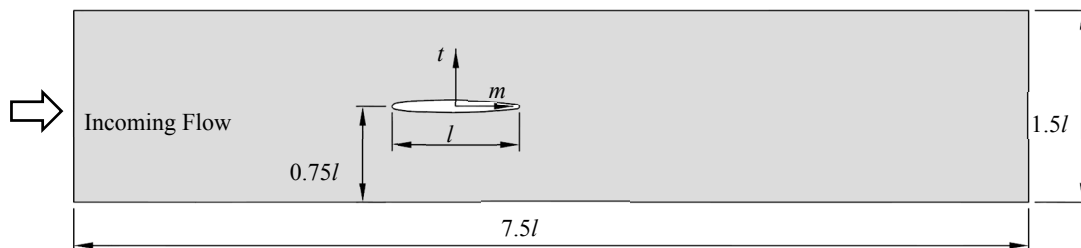


Figure 2. Flow domain for computational fluid dynamics (CFD) simulation.

3. Methods

3.1. Numerical Model of Turbulent Flow

In this study, the Reynolds-averaged Navier–Stokes (RANS) equations were used to solve the turbulent flow. Considering the turbulence isotropic assumption and rotating/curvature insensitivity of eddy viscosity models, the v^2 - f model, which can be more suitable especially for the viscous flow separation from a curved hydrofoil surface, was used. The v^2 - f model was based on the turbulence kinetic energy k equation, dissipation rate ε equation, velocity variance scale $\overline{v^2}$ equation, and the elliptic relaxation function f . It can be expressed as [41–43]:

$$\frac{\partial(\rho k)}{\partial t} + \frac{\partial(\rho u_i k)}{\partial x_i} = P - \rho\varepsilon + \frac{\partial}{\partial x_j} \left[\left(\mu + \frac{\mu_t}{\sigma_k} \right) \frac{\partial k}{\partial x_j} \right] + S_k \quad (3)$$

$$\frac{\partial(\rho k)}{\partial t} + \frac{\partial(\rho u_i k)}{\partial x_i} = \frac{C'_{\varepsilon 1} P - C_{\varepsilon 2} \rho \varepsilon}{T} + \frac{\partial}{\partial x_j} \left[\left(\mu + \frac{\mu_t}{\sigma_\varepsilon} \right) \frac{\partial \varepsilon}{\partial x_j} \right] + S_\varepsilon \quad (4)$$

$$\frac{\partial(\rho\overline{v^2})}{\partial t} + \frac{\partial(\rho\overline{v^2}u_i)}{\partial x_i} = \rho kf - 6\rho\overline{v^2}\frac{\varepsilon}{k} + \frac{\partial}{\partial x_j} \left[\left(\mu + \frac{\mu_t}{\sigma_k} \right) \frac{\partial\overline{v^2}}{\partial x_j} \right] + S_{\overline{v^2}} \quad (5)$$

$$f - L^2 \frac{\partial^2 f}{\partial x_j^2} = (C_1 - 1) \frac{2k - 3\overline{v^2}}{3kT} + C_2 \frac{P}{\rho k} + \frac{5\overline{v^2}}{kT} + S_f \quad (6)$$

where $C_1, C_2, C_{\varepsilon 1}, C'_{\varepsilon 1}, C_{\varepsilon 2}, C_\eta, C_\mu,$ and C_L are model constants; σ_k and σ_ε are the turbulent Prandtl numbers; and $S_k, S_\varepsilon, S_{\overline{v^2}},$ and S_f are source terms. Term T is the turbulent time scale and L is the turbulent length scale:

$$T' = \max \left[\frac{k}{\varepsilon}, 6\sqrt{\frac{\nu}{\varepsilon}} \right] \quad (7)$$

$$T = \min \left[T', \frac{\alpha}{\sqrt{3}} \frac{k}{\overline{v^2} C_\mu \sqrt{2S^2}} \right] \quad (8)$$

$$L' = \min \left[\frac{k^{3/2}}{\varepsilon}, \frac{1}{\sqrt{3}} \frac{k^{3/2}}{\overline{v^2} C_\mu \sqrt{2S^2}} \right] \quad (9)$$

$$L = C_L \max \left[L', C_\eta \left(\frac{\nu^3}{\varepsilon} \right)^{1/4} \right] \quad (10)$$

where α is a model constant, ν is the kinematic viscosity, and S is the strain rate tensor. Thus, the turbulent viscosity μ_t can be expressed as

$$\mu_t = \rho C_\mu \overline{v^2} T. \quad (11)$$

All the default values of the model constants are listed in Table 1. Based on $C_{\varepsilon 1}$, the value of $C'_{\varepsilon 1}$ can be calculated by

$$C'_{\varepsilon 1} = C_{\varepsilon 1} \left(1 + 0.045 \sqrt{\frac{k}{\overline{v^2}}} \right). \quad (12)$$

Table 1. Default value of the model constants in the v^2 - f turbulence model.

Constant	α	C_1	C_2	$C_{\varepsilon 1}$	$C_{\varepsilon 2}$	C_η	C_μ	C_L	σ_k	σ_ε
Value	0.6	1.4	0.3	1.4	1.9	70	0.22	0.23	1.0	1.3

3.2. CFD Setup

Based on the setting of the turbulent flow, the flow domain was discretized using unstructured mesh elements as shown in Figure 3. The mesh scheme was determined by an independence check and had 64,868 nodes in total. Considering the usage of the v^2 - f turbulence model, the near-wall mesh in the boundary layer was checked and refined with three prism layers (first layer height 1×10^{-4} mm, growth rate 1.2). The y^+ value was in the range of 0.08–6.86, which fits the requirement of a direct near-wall solution. In the simulation, the Reynolds number Re was set to 5×10^5 with the incidence angle between 0 and 6 degrees. The boundary conditions were set as follows: Firstly, the velocity inlet boundary was set at the inflow, the velocity was perpendicular to the inlet boundary, and the pressure followed the Neumann condition. Secondly, the pressure boundary was set at the outflow with average 0 Pa, and the velocity followed the Neumann condition. Thirdly, the no-slip condition was applied on the wall boundaries including the upper domain boundary, lower domain boundary, and the foil surface. Moreover, to simplify the 3D case to 2D, symmetry boundaries were given perpendicular to the 2D domain plane. The fluid medium was set as water at 20 °C with density 1×10^3 kg/m³ and dynamic viscosity 1.01×10^{-3} Pa·s. The steady-state simulation was conducted with a maximum

iteration number of 1000, and the convergence criterion was set to 1×10^{-5} . The transient-state simulation was conducted based on the steady-state simulation. For a better convergence performance and timely flow regime resolution, the total time and time step were determined based on the Reynolds number and Courant number. Finally, the total time was set as 2 s with a constant time step of 2×10^{-5} s which can be suitable in this case.

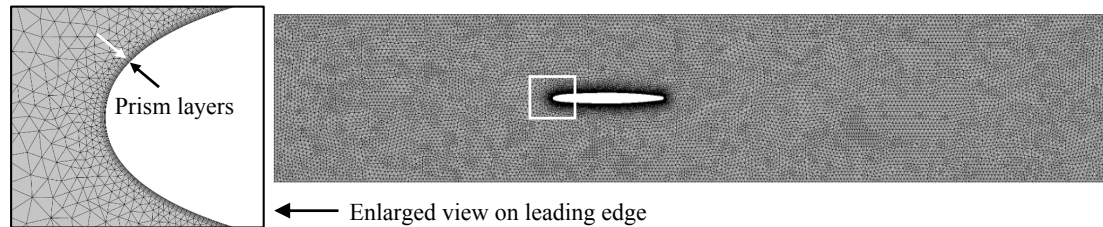


Figure 3. Schematic map of mesh elements with an enlarged view on LE.

3.3. Brief Introduction to the Diffusion Angle Integral Method

The Diffusion-angle Integral (DI) method [40] can improve the cavitation performance by changing the geometry of the foil LE. First, the DI method requires the geometric deconstruction of the foil, as shown in Figure 4. The shape of the arc and diffusion section of the foil changes rapidly. So, the DI method was mainly used to design the geometry of the foil LE. In this study, the length of the design section was $0.15l$ along the length of the meanline, which is divided into circular and integral sections. Through the DI method, the number of design parameters can be simplified to three, which greatly improves the design efficiency. The DI method is mainly divided into five steps as follows:

1. Providing the long/short axis ratio $R_{ab} = a_{LE}/b_{LE}$;
2. Based on R_{ab} , scaling the ellipse arc into an arc;
3. Providing the diffusion angle γ_s and calculating the scaled LE arc r_{LE} ;
4. Providing the thickness integral coefficient B (the change rate of Part 2 in Figure 4) and integrating the thickness diffusion part;
5. Based on R_{ab} , scaling the designed arc back to an ellipse arc.

Based on the steps above, the LE ellipse arc can be calculated under coordinate scaling:

$$a_{LE} = R_{ab} \frac{t_{O'} - 2m_{O'} \tan \gamma_s}{2(\sin \gamma_s \tan \gamma_s - \tan \gamma_s + \cos \gamma_s)} \quad (13)$$

$$b_{LE} = \frac{a_{LE}}{R_{ab}} \quad (14)$$

where $t_{O'}$ is the thickness at O' and $m_{O'}$ is the m position at O' . The increase in t at the thickness diffusion section can be calculated by

$$\Delta t = C_s \int_{m_A}^{m_{O'}} \tan \gamma(m) dm \quad (15)$$

where m_A is the m position at point A , C_s is the scale factor, and $\gamma(m)$ is the thickness integral expression which is defined as

$$\gamma(m) = \left(\frac{m_{O'} - m}{m_{O'} - m_A} \right)^B. \quad (16)$$

The variation law at thickness diffusion section can be controlled by the coefficient B . Applying DI method can be simple by following the steps above but the detailed mathematical deduction process of the DI method is complex. Hence, only the brief introduction is put here and the detail of DI method can be found in Ref. [40].

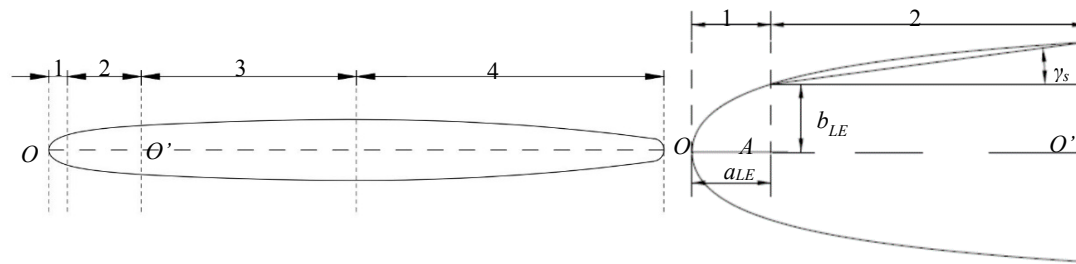


Figure 4. Geometry deconstruction and parameters of the Diffusion angle Integral method: 1—Elliptical arc section; 2—Thickness diffusion section; 3—Thickness transition section; 4—Thickness reduction section.

3.4. Orthogonal Testing

The orthogonal test method can be used instead of large scale comprehensive test with fewer test times. In this paper, 25 tests (3 factors and 5 levels) were used in the design of orthogonal test. The optimum values of 3 parameters in the DI method under different incidence angles were analyzed. The factor levels of R_{ab} , γ_s , B are shown in Table 2.

Table 2. Factor levels.

Level	Factor		
	R_{ab}	γ_s [degree]	B
1	1	1	1
2	1.5	2	2
3	2	3	3
4	2.5	4	4
5	3	5	5

In the process of flow, the dimensionless pressure coefficient C_p is used to characterize the surface pressure of the foil:

$$C_p = \frac{p - p_\infty}{\frac{1}{2}\rho V_\infty^2} \quad (17)$$

where p is the foil surface pressure, p_∞ is the reference position average pressure (calculation domain inlet), and V_∞ is the reference position average speed (calculation domain inlet). Typically, the number of cavitation number C_σ is defined as:

$$C_\sigma = \frac{p_\infty - p_v}{\frac{1}{2}\rho V_\infty^2}, \quad (18)$$

when cavitation begins, we have $p_{min} = p_v$. Therefore, the minimum pressure coefficient C_{pmin} on the foil surface is negatively correlated with the inception cavitation number $C_{\sigma i}$:

$$-C_{pmin} = C_{\sigma i}. \quad (19)$$

The minimum pressure coefficient of the foil surface C_{pmin} was chosen as the evaluation index. As shown in Table 3, the minimum pressure coefficients $C_{p\alpha}$ of foils with different incidence angles of 0, 3, and 6 degrees were obtained by numerical simulation. Then, the range analyses were conducted based on the results of orthogonal test as shown in Table 4. $K_1 \sim K_5$ and $k_1 \sim k_5$ are the polar difference values and averaged polar difference values, respectively. R is the range value based on orthogonal test.

Table 3. Orthogonal test table with factors, levels and test values.

Order Number	R_{ab}	γ_s [deg]	B	C_{p0}	C_{p3}	C_{p6}
1	1	1	1	-1.4987	-2.889	-4.4240
2	1	2	2	-1.4316	-2.8391	-4.4486
3	1	3	3	-1.3561	-2.8080	-4.5451
4	1	4	4	-1.2756	-2.7677	-4.5856
5	1	5	5	-1.1910	-2.7169	-4.5187
6	1.5	1	2	-1.0299	-2.1063	-3.5227
7	1.5	2	3	-0.9875	-2.0877	-3.5436
8	1.5	3	4	-0.9407	-2.0723	-3.5969
9	1.5	4	5	-0.8888	-2.0526	-3.5870
10	1.5	5	1	-0.8322	-2.0367	-3.6896
11	2	1	3	-0.7890	-1.7245	-3.1430
12	2	2	4	-0.7610	-1.7185	-3.1881
13	2	3	5	-0.7299	-1.7103	-3.2384
14	2	4	1	-0.6940	-1.7091	-3.2879
15	2	5	2	-0.6526	-1.7020	-3.3610
16	2.5	1	4	-0.6439	-1.5140	-3.0710
17	2.5	2	5	-0.6262	-1.5180	-3.1082
18	2.5	3	1	-0.6048	-1.5189	-3.1723
19	2.5	4	2	-0.5783	-1.5251	-3.2313
20	2.5	5	3	-0.5467	-1.5277	-3.3146
21	3	1	5	-0.5469	-1.4048	-3.1355
22	3	2	1	-0.5357	-1.4083	-3.1153
23	3	3	2	-0.5216	-1.4109	-3.2224
24	3	4	3	-0.5027	-1.4163	-3.2881
25	3	5	4	-0.4768	-1.4230	-3.3829

Table 4. Range analysis results.

ParamETERS	C_{p0}			C_{p3}			C_{p6}		
	R_{ab}	γ_s [deg]	B	R_{ab}	γ_s [deg]	B	R_{ab}	γ_s [deg]	B
K_1	-9.0567	-6.3002	-6.0576	-14.144	-9.8917	-9.8353	-20.095	-15.252	-15.524
K_2	-6.5729	-6.1712	-6.1082	-10.546	-9.8318	-9.8667	-15.855	-15.314	-15.609
K_3	-5.3795	-6.0521	-6.0855	-8.8359	-9.8091	-9.8531	-14.194	-15.587	-15.642
K_4	-4.7500	-5.8966	-6.0104	-7.9727	-9.7685	-9.7886	-13.778	-15.725	-15.619
K_5	-4.3877	-5.7268	-5.8853	-7.5234	-9.7216	-9.6791	-13.880	-15.924	-15.409
k_1	-1.8114	-1.2601	-1.2115	-2.8289	-1.9783	-1.9671	-4.0190	-3.0503	-3.1048
k_2	-1.3146	-1.2342	-1.2216	-2.1093	-1.9664	-1.9733	-3.1711	-3.0629	-3.1217
k_3	-1.0759	-1.2104	-1.2171	-1.7672	-1.9618	-1.9706	-2.8388	-3.1175	-3.1284
k_4	-0.9500	-1.1793	-1.2021	-1.5945	-1.9537	-1.9577	-2.7556	-3.1450	-3.1238
k_5	-0.8775	-1.1454	-1.1771	-1.5047	-1.9443	-1.9358	-2.7760	-3.1848	-3.0817
R	0.9338	0.1147	0.0446	1.3242	0.0340	0.0375	1.2634	0.1345	0.0467

It can be seen from Tables 2 and 3 that R_{ab} has the greatest influence on the minimum pressure coefficient C_p of the foil surface. When the incidence angle is 0 degree, the optimal parameter combination is $R_{ab} = 3$, $\gamma_s = 5$, and $B = 4$. When the incidence angle is 3 degrees, the optimal parameter combination is $R_{ab} = 3$, $\gamma_s = 2$, and $B = 1$. When the incidence angle is 6 degrees, the optimal parameter combination is $R_{ab} = 2.5$, $\gamma_s = 1$, and $B = 4$. The optimal parameter combination given by the orthogonal testing is the basis for the next step in finding the optimal design.

4. Optimization

4.1. Global Dynamic Criterion Algorithm

To further optimize the design, an improved hill climbing algorithm with heuristic parallel characteristics was proposed in this paper. The algorithm was used to search for the distribution of multiple local optimal values in a certain area. It can optimize the design parameters of foil LE.

The optimal value of the design parameters of foil LE is searched quickly and efficiently. The minimum pressure coefficient of foil surface can be improved. The algorithm includes the following steps:

(1) The algorithm is based on hill climbing algorithm. Firstly, 10 parameter combinations denoted as F_n ($n = 1, 2, 3 \dots, 10$) are randomly generated near the optimal values obtained by the orthogonal experiments of 3 parameters R_{ab} , γ_s , B in the DI method. The corresponding foil is numerically simulated for each set of parameters F_n . Three different cases of incidence angle 0, 3 and 6 degrees are calculated respectively. The minimum pressure coefficient $C_{p\alpha}$ of the foil LE shape under each incidence angle is obtained. Therefore, the minimum pressure coefficient obtained from the LE parameters of each group is defined as C_{pmin} :

$$C_{pmin} = I \times C_{p0} + j \times C_{p3} + k \times C_{p6} \quad (i + j + k = 1). \quad (20)$$

When focus on cavitation performance at 0 degree of incidence angle, here are $i = 0.8$, $j = 0.1$, $k = 0.1$. For 3 degrees, here are $i = 0.1$, $j = 0.8$, $k = 0.1$. For 6 degrees, here are $i = 0.1$, $j = 0.1$, $k = 0.8$.

(2) We then set the initial decision condition C_{pt} . We decide whether the C_{pmin} obtained from each set of parameters F_n satisfies the criteria. If $C_{pmin} \geq C_{pt}$, we keep this set of parameters and search in the neighborhood of each parameter. The search range should not exceed 5% of the total parameter range. If $C_{pmin} < C_{pt}$, we discard this set of parameters, and re-generate a group for the next round of the search. The optimal value of each search is T_n ($n = 1, 2, 3, \dots, 10$).

(3) When searching in a small neighborhood, the new set of parameters F'_n will be used for the foil LE design. A new two-dimensional foil is thus obtained. Three different cases of incidence angle—0, 3, and 6 degrees—are calculated. The minimum pressure coefficient $C_{p\alpha}$ of the foil LE shape under each incidence angle is obtained. Taking the case of 0 degree as an example, C'_{pmin} is obtained using Equation (16). For each group of F'_n , the optimal T_1 value obtained from the first search is the criterion for the second search. If $C'_{pmin} \geq T_1$, we keep this set of parameters and search in the neighborhood of the new set of parameters F'_n . The search range should not exceed 5% of the total parameter range. If $C'_{pmin} < T_1$, we discard this set of parameters, and re-generate a group for the next round of the search.

(4) For the third search round, it is necessary to continue to change the criteria T_3 . It is changed to the weighted value of the optimal value T_1 of the first search round and the optimal value T_2 of the second search round. T_3 is defined as:

$$T_3 = p \times T_1 + q \times T_2 \quad (p + q = 1) \quad (21)$$

The purpose of changing the criteria is to continuously improve the goal of optimization. Here, $p = 0.4$ and $q = 0.6$.

(5) In order to avoid falling into the local optimal solution, we set a small probability to terminate the current search. The termination probability Y and iteration number x have a certain functional relationship. The function has the following characteristics. With increasing x , the termination probability Y increases. When iteration number $x \rightarrow +\infty$, termination probability $Y \rightarrow 1$. According to the above characteristics, the function can be written as

$$\begin{cases} Y(x) = 0, x < 3 \\ Y(x) = \left[-e^{\left(\frac{b-x}{a}\right)} + c \right] \%, x \geq 3 \end{cases} \quad (22)$$

where a , b , and c are constants. The function can adjust the specific values of a , b , and c according to the maximum iteration number, so as to adjust the distribution of the termination probability. Here, the values in this study are as follows: $a = 2.8$, $b = 10$, and $c = 1$.

(6) The maximum iteration number in this article is set to 50 to have a balance between searching time and improvement effect. Repeat the above steps until reach the maximum iteration number, and finally get the global optimal solution. The optimum design parameters of foil LE at 0 degree, 3 degrees and 6 degrees of incidence angles are obtained.

4.2. Comparison of Foil Geometry

After optimization, the optimal geometries were get respectively on 0 degree, 3 degrees and 6 degrees. As shown in Figure 5, differences can be found in the range of 0–0.15 m/l . The optimal geometry for 0 degree has the smallest thickness values within 0–0.15 m/l . The optimal geometry for 6 degrees has the largest thickness values within 0–0.15 m/l . The differences of geometry showed the adaptability of incoming flow striking and local separation caused by incidence angle. The mechanism was analyzed in detail in the next section.

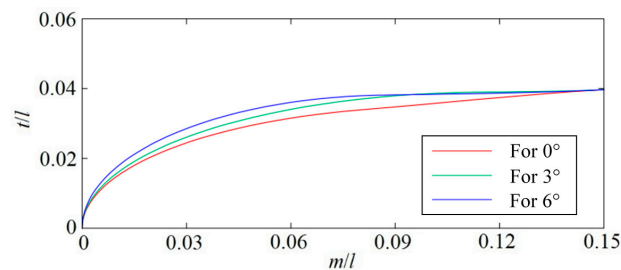


Figure 5. Schematic diagram of the optimal foil LE shape for 0, 3, and 6 degrees.

5. Results and Discussion

5.1. Comparison of $-C_{pmin}$ and Lift/Drag Ratio

The $-C_{pmin}$ of the original foil and the optimal three foils were compared, as shown in Figure 6. It can be seen from the Figure that the $-C_{pmin}$ of the optimal foils and the original foil at the 0 degree is similar with only difference of 1.2%. However, with the increase of the incidence angle, the optimal foils are lower than the original foil at 3 degrees and 6 degrees, which decreases by 11.4% and 14.5% respectively. It shows that the cavitation performance of the optimal foil at 3°~6° is improved. Comparing the three optimal foils, it can be seen that the $-C_{pmin}$ of the optimal for 0 degree' foil are lower in the range of 0~3 degrees, but higher at 6 degrees' incidence angle. However, the $-C_{pmin}$ of the optimal for 6 degrees' foil are lower at 6 degrees' incidence angle, but higher in the range of 0~3 degrees. Generally, the application of the DI method and GDC algorithm on optimizing the foil geometry can effectively improve the cavitation performance at large incidence angle. The foil with better cavitation performance can be obtained by focusing on a certain incidence angle, but the performance of both large and small incidence angles is difficult to be considered at the same time. Figure 7 compared the lift/drag ratio F_L/F_D of the original foil and the optimal foils. From the comparison of F_L/F_D , it can be seen that the F_L/F_D of the optimal foils are slightly lower than that of the original foil, but the overall difference is very small. The minimum difference is 0.1% and the maximum difference is 5%. The results showed that the performance of foil is not affected after optimization.

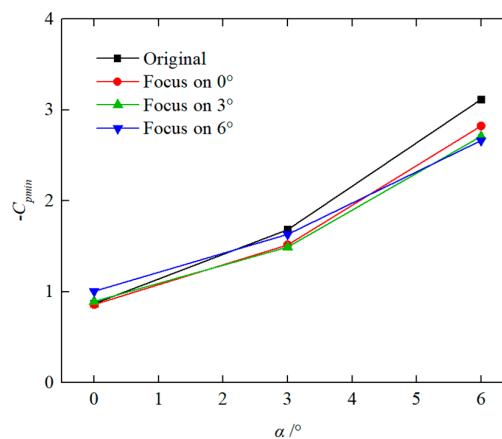


Figure 6. Comparison of $-C_{pmin}$ values.

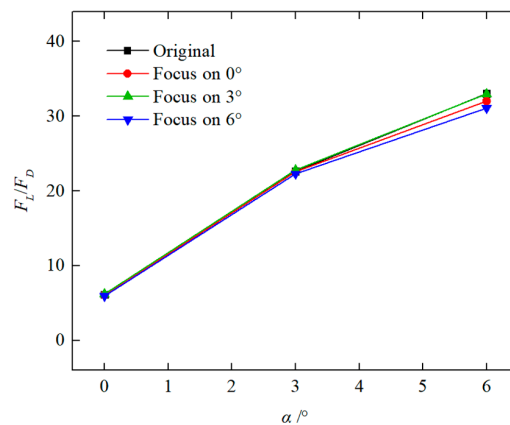


Figure 7. Comparison of lift/drag ratio F_L/F_D .

5.2. Pressure Distribution on the Foil Surface

Figure 8 shows a comparison of the surface pressure distribution curves of the three optimal foils under different incidence angles. It can be seen from the figure that the position of the lowest pressure point obtained by different LE shapes at the same incidence angle is relatively small. The lowest pressure coefficient has a certain difference. In Figure 8a, where $\alpha = 0$ degree, the optimal foil for 0 degree has the gentlest pressure drop on LE, while the optimal foil for 6 degrees has the most sudden pressure drop on LE. This shows that the optimal foil for 0 degree fits the incidence angle of 0 degree the best. The opposite relationship can be found in Figure 8c. However, the situation becomes complex in Figure 8b. At $\alpha = 3$ degrees, the optimal foil for 3 degrees fitted the incidence angle of 3 degrees the best. The optimal foil for 0 degree also performed well at the incidence angle of 3 degrees. The optimal foil for 6 degrees was the worst and had the minimum $-C_{pmin}$. Generally, the optimal design for a specific incidence angle has a gentler pressure drop on the LE. The cavitation scale would consequently be smaller after the design optimization.

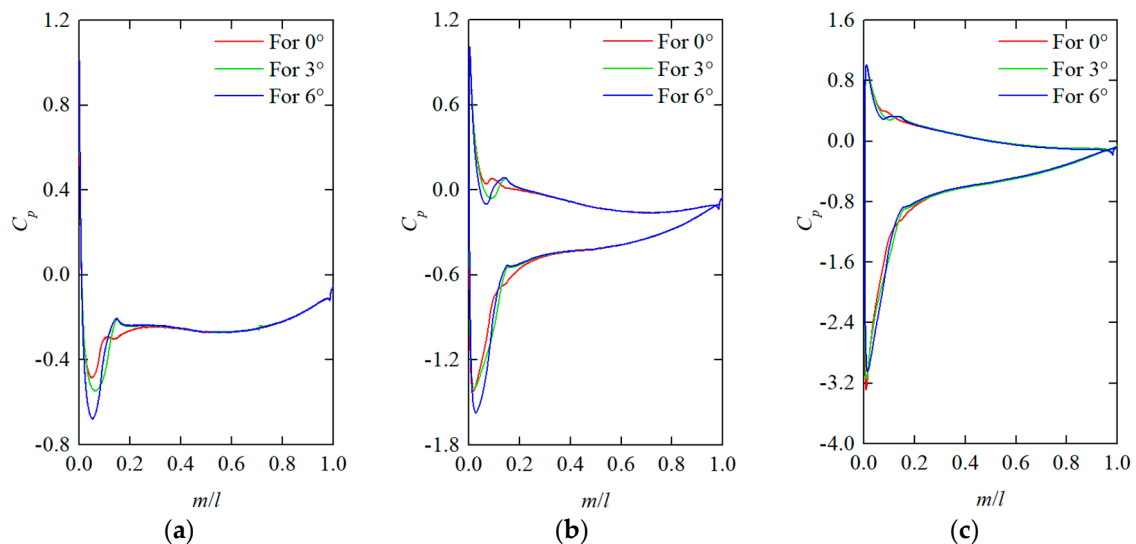


Figure 8. Surface pressure distribution curves of the three optimal foils under different incidence angles: (a) $\alpha = 0^\circ$; (b) $\alpha = 3^\circ$; (c) $\alpha = 6^\circ$.

5.3. Flow Field around the Foil

The pressure and velocity vectors at the LE of the three optimal foils were compared and analyzed, as shown in Figure 9 and Figure 10. It can be seen from Figure 9 that when the incidence angle is 0 degree, the low-pressure area of the LE of the foil optimal for 0 degree is smaller. With the change of

the LE geometry, the low-pressure zones of the foils optimal for 3 degrees and for 6 degrees gradually increase. After increasing the incidence angle, the pressure distributions of the three optimal foils' LE are similar. By analyzing the velocity vector, it is found that the three foils each have the smallest flow separation at their respective optimal incidence angle. This is because the gradient of geometric change is slower under the corresponding incidence angle. The local separation of the optimal foil LE is improved obviously. The pressure drop near the LE slows down. The shape of the foil LE can be adapted to the direction of incoming flow, making the flow more suitable for the foil. It is thus shown that the cavitation performances of the optimal foils at various incidence angles can be significantly improved by using the DI method and the GDC algorithm.

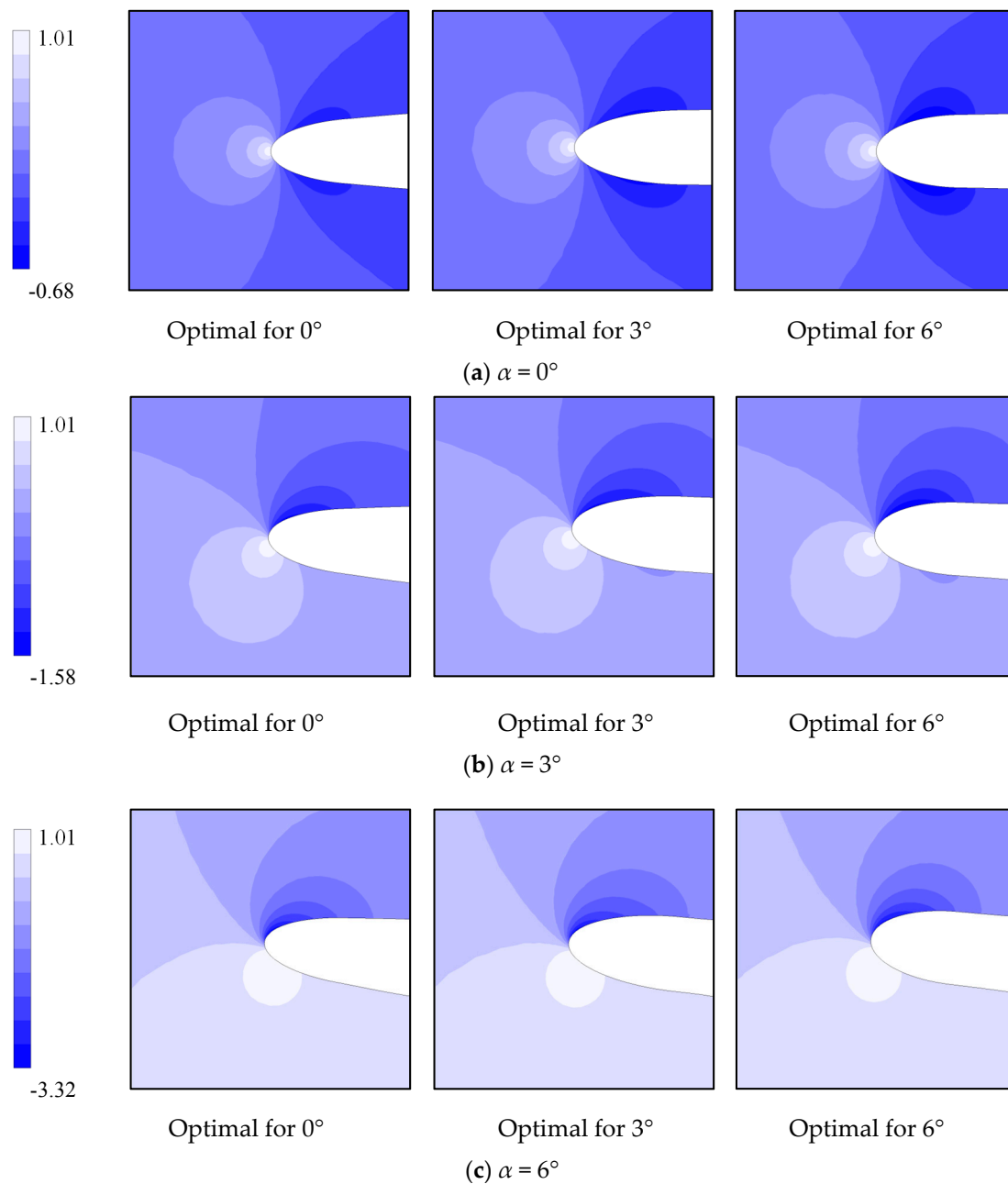


Figure 9. Contour of the dimensionless pressure coefficient C_p .

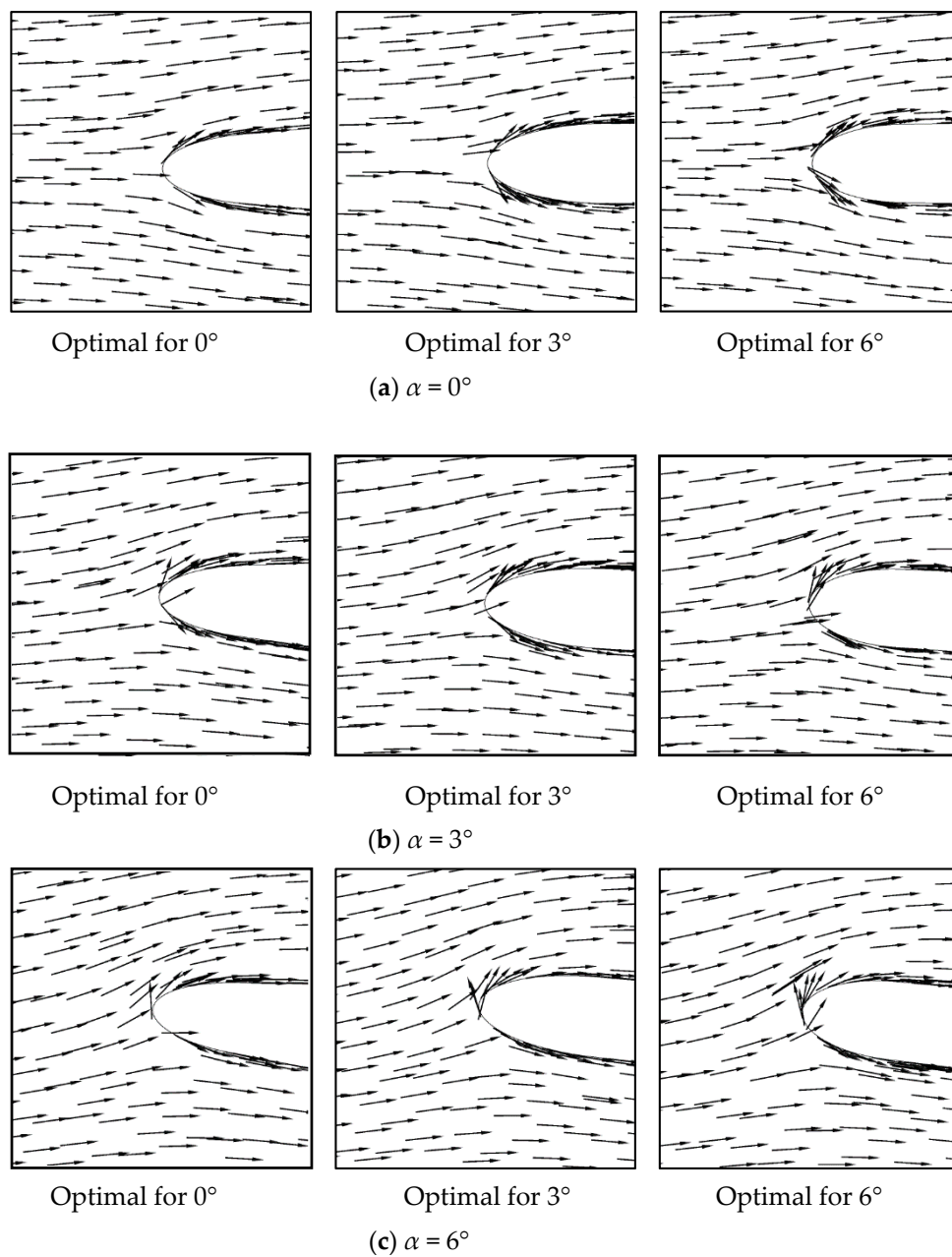


Figure 10. Velocity vectors around the foils.

6. Conclusions

According to the study above, the following three conclusions can be drawn:

(a) The global dynamic-criterion algorithm based on the improved hill-climbing algorithm was introduced. It can initially filter the input parameters/conditions, run in a parallel mode, and set a small probability for falling into the local optimum trap. In this optimization of the cavitation performance of foils or impeller blades, the relationship between cavitation behavior and foil/blade profile is strongly nonlinear. Thus, the global dynamic criterion algorithm provided a reasonable and convenient solution for this cavitation optimization problem.

(b) Several typical methods and some new methods were combined for the optimization. The typical methods include the CFD simulation for turbulent flow and the orthogonal test. The new methods include the Diffusion-angle Integral method and the global dynamic-criterion algorithm. They worked together to search the optimal geometry for improving the cavitation performance for 0, 3 and 6 degrees' incidence angles.

(c) The front 15% geometry was re-designed with slight changing on geometry and impressive enhancement on cavitation performance. The $-C_{pmin}$ of the optimal foils was improved by 1.2%, 11.4% and 14.5% at 0 degree, 3 degrees and 6 degrees comparing with the original foil. In the design range, different parameter values of Diffusion-angle Integral method caused different geometries. The geometries fitted the incoming flow better with smaller scale LE separation and gentler pressure drop. The cavitation performance was enhanced at different incidence angles.

Above all, the geometry re-design around leading-edge can efficiently improve the cavitation performance of hydrofoil. This study provided a successful work for applying anti-cavitation design to the impellers of hydraulic turbomachinery. This study will be helpful for readers who need the improvement of cavitation performance for foils and impellers.

Author Contributions: Methodology, D.Z. and R.T.; Investigation, D.Z.; Writing-Original Draft Preparation, D.Z.; Writing-Review & Editing, R.X.; Supervision, F.W.; Funding Acquisition, R.T., R.X. and F.W.

Funding: This research was funded by National Natural Science Foundation of China, grant number 51836010; National Natural Science Foundation of China, grant number 51879265; China Postdoctoral Science Foundation, grant number 2018M640126.

Conflicts of Interest: The authors declare no conflict of interest.

References

1. Hammitt, F.G. *Cavitation and Multiphases Flow Phenomena*, 1st ed.; McGraw-Hill: New York, NY, USA, 1980; ISBN 9780070259072.
2. Luo, X.; Ji, B.; Tsujimoto, Y. A review of cavitation in hydraulic machinery. *J. Hydrodyn.* **2016**, *28*, 335–358. [[CrossRef](#)]
3. Pan, Z.Y.; Yuan, S.Q. *Fundamentals of Cavitation in Pumps*, 1st ed.; Jiangsu University Press: Zhenjiang, China, 2013.
4. Bishop, R.J.; Totten, G.E. Effect of pump inlet conditions on hydraulic pump cavitation: A review. *ASTM Spec. Tech.* **2001**, *339*, 318–332.
5. Lauterborn, W.; Bolle, H. Experimental investigation of cavitation-bubble collapse in the neighbourhood of a solid boundary. *J. Fluid Mech.* **1975**, *72*, 391–399. [[CrossRef](#)]
6. Wang, G.; Liu, S.; Shintani, M. Study on Cavitation Damage Characteristics around a Hollow-Jet Valve. *JSME Int. J.* **1999**, *42*, 649–657. [[CrossRef](#)]
7. Visser, F.C.; Backx, J.J.M.; Geerts, J. Pump impeller lifetime improvement through visual study of leading-edge cavitation. In Proceedings of the International Pump Users Symposium, Houston, TX, USA, 3–5 March 1998.
8. Tao, R.; Xiao, R.; Zhu, D. Predicting the inception cavitation of a reversible pump-turbine in pump mode. In Proceedings of the 9th International Symposium on Cavitation, Lausanne, Switzerland, 6–10 December 2015.
9. Ruan, H.; Luo, X.; Liao, W. Effects of low pressure edge thickness on cavitation performance and strength for pump-turbine. *Trans. Chin. Soc. Agric. Eng.* **2015**, *31*, 32–39.
10. Adhikari, R.; Vaz, J.; Wood, D. Cavitation Inception in Crossflow Hydro Turbines. *Energies* **2016**, *9*, 237. [[CrossRef](#)]
11. Anaka, T.; Tsukamoto, H. Transient behavior of a cavitating centrifugal pump at rapid change in operating conditions-Part 2: Transient phenomena at pump startup/shutdown. *J. Fluids Eng.* **1999**, *121*, 850–856.
12. Balasubramanian, R.; Sabini, E.; Bradshaw, S. Influence of impeller leading edge profiles on cavitation and suction performance. In Proceedings of the 27th International Pump Users Symposium, Houston, TX, USA, 12–15 September 2011.
13. Obeid, S.; Jha, R.; Ahmadi, G. RANS Simulations of Aerodynamic Performance of NACA 0015 Flapped Airfoil. *Fluids* **2017**, *2*, 2. [[CrossRef](#)]

14. Wang, G.; Ostoja-Starzewski, M. Large eddy simulation of a sheet/cloud cavitation on a NACA0015 hydrofoil. *Appl. Math. Model.* **2007**, *31*, 417–447. [[CrossRef](#)]
15. Neill, G.D.; Reuben, R.L.; Sandford, P.M. Detection of incipient cavitation in pumps using acoustic emission. *J. Process. Mech. Eng.* **1997**, *211*, 267–277. [[CrossRef](#)]
16. Fukaya, M.; Okamura, T.; Tamura, Y. Prediction of cavitation performance of axial flow pump by using numerical cavitating flow simulation with bubble flow model. In Proceedings of the 5th International Symposium on Cavitation, Osaka, Japan, 1–4 November 2003.
17. Barre, S.; Rolland, J.; Boitel, G. Experiments and modeling of cavitating flows in venturi: Attached sheet cavitation. *Eur. J. Mech. B/Fluids* **2009**, *28*, 444–464. [[CrossRef](#)]
18. Acosta, A.J.; Tsujimoto, Y.; Yoshida, Y. Effects of leading edge sweep on the cavitating characteristics of inducer pumps. *Int. J. Rotating Mach.* **2007**, *7*, 397–404. [[CrossRef](#)]
19. Numachi, F.; Oba, R.; Chida, I. Effect of surface roughness on cavitation performance of hydrofoils-report 1. *J. Basic Eng.* **1965**, *87*, 495–502. [[CrossRef](#)]
20. Yao, Z.; Xiao, R.; Wang, F. Numerical investigation of cavitation improvement for a francis turbine. In Proceedings of the 9th International Symposium on Cavitation, Lausanne, Switzerland, 1–5 December 2015.
21. Kinnas, S.A. Non-Linear Corrections to the Linear Theory for the Prediction of the Cavitating Flow around Hydrofoils. Ph.D. Thesis, Massachusetts Institute of Technology, Boston, MA, USA, 1985.
22. Tao, R.; Xiao, R.; Farhat, M. Effect of leading edge roughness on cavitation inception and development on a thin hydrofoil. *J. Drain. Irrig. Mach. Eng.* **2017**, *35*, 921–926.
23. Bouziad, Y.A. Physical modelling of leading edge cavitation: Computational methodologies and application to hydraulic machinery. *EPFL* **2005**, 3353. [[CrossRef](#)]
24. Ausoni, P. Turbulent vortex shedding from a blunt trailing edge hydrofoil. *EPFL* **2009**. [[CrossRef](#)]
25. Coutier-Delgosha, O.; Reboud, J.L.; Delannoy, Y. Numerical simulation of the unsteady behavior of cavitating flows. *Int. J. Numer. Methods Fluids* **2003**, *42*, 527–548.
26. Kunz, R.F.; Boger, D.A.; Stinebring, D.R. A preconditioned Navier–Stokes method for twophase flows with application to cavitation prediction. *Comput. Fluids* **2000**, *29*, 849–875. [[CrossRef](#)]
27. Yang, W.; Xiao, R.; Wang, F. Influence of splitter blades on the cavitation performance of a double suction centrifugal pump. *Adv. Mech. Eng.* **2014**, *6*. [[CrossRef](#)]
28. Gopalan, S.; Katz, J. Flow structure and modeling issues in the closure region of attached cavitation. *Phys. Fluids* **2000**, *12*, 895–911. [[CrossRef](#)]
29. Luo, X.; Zhang, Y.; Peng, J. Impeller inlet geometry effect on performance improvement for centrifugal pumps. *J. Mech. Sci. Technol.* **2008**, *22*, 1971–1976. [[CrossRef](#)]
30. Tan, L.; Cao, S.; Wang, Y. Numerical Simulation of Cavitation in a Centrifugal Pump at Low Flow Rate. *Chin. Phys. Lett.* **2012**, *29*, 014702. [[CrossRef](#)]
31. Ting, C.K. On the mean convergence time of multi-parent genetic algorithms without selection. *Adv. Artif. Life* **2005**, 403–412.
32. Akbari, R.; Ziarati, K. A multilevel evolutionary algorithm for optimizing numerical functions. *Int. J. Ind. Eng. Comput.* **2011**, *2*, 419–430. [[CrossRef](#)]
33. Whitley, D. A genetic algorithm tutorial. *Stat. Comput.* **1994**, *4*, 65–85. [[CrossRef](#)]
34. Colomi, A.; Dorigo, M.; Maniezzo, V. Ant system for job-shop scheduling. *Oper. Res. Stat. Comput. Sci.* **1994**, *34*, 39–53.
35. Cormen, T.H.; Leiserson, C.E.; Rivest, R.L. *Introduction to Algorithms*, 2nd ed.; McGraw-Hill: New York, NY, USA, 2001.
36. Huang, L.; Huang, P.G.; Lebeau, R.P. Optimization of aifoil flow control using a genetic algorithm with diversity control. *J. Aircr.* **2007**, *44*, 1337–1349. [[CrossRef](#)]
37. Liu, H.; Wang, K.; Yuan, S. Multicondition Optimization and Experimental Measurements of a Double-Blade Centrifugal Pump Impeller. *J. Fluids Eng.* **2013**, *135*, 111031. [[CrossRef](#)] [[PubMed](#)]
38. Liu, L.; Zhu, B.; Bai, L. Parametric design of an ultrahigh-head pump-turbine runner based on multiobjective optimization. *Energies* **2017**, *10*, 1169. [[CrossRef](#)]
39. Liu, M.; Tan, L.; Cao, S. Design method of controllable blade angle and orthogonal optimization of pressure rise for a multiphase pump. *Energies* **2018**, *11*, 1048. [[CrossRef](#)]

40. Tao, R.; Xiao, R.; Wang, F. Improving the cavitation inception performance of a reversible pump-turbine in pump mode by blade profile redesign: Design concept, method and applications. *Renew. Energy* **2019**, *133*, 325–342. [[CrossRef](#)]
41. Behnia, M.; Parneix, S.; Shabany, Y. Numerical study of turbulent heat transfer in confined and unconfined impinging jets. *Int. J. Heat Fluid Flow* **1999**, *20*, 1–9. [[CrossRef](#)]
42. Durbin, P.A. Separated Flow Computations with the $k-\epsilon-v2$ Model. *AIAA J.* **1995**, *33*, 659–664. [[CrossRef](#)]
43. Parneix, S.; Durbin, P.A.; Behnia, M. Computation of 3-D Turbulent Boundary Layers Using the V2F Model. *Flow Turbul. Combust.* **1998**, *60*, 19–46. [[CrossRef](#)]



© 2018 by the authors. Licensee MDPI, Basel, Switzerland. This article is an open access article distributed under the terms and conditions of the Creative Commons Attribution (CC BY) license (<http://creativecommons.org/licenses/by/4.0/>).